

Article

# Influence of Nanocrystalline Palladium Morphology on Alkaline Oxygen Reduction Kinetics

Eliran Hamo <sup>†</sup>, Avichay Raviv <sup>†</sup> and Brian A. Rosen <sup>\* </sup>

Department of Materials Science and Engineering, Tel Aviv University, Ramat Aviv 69978001, Israel

\* Correspondence: barosen@post.tau.ac.il

† Authors with equal contribution.

Received: 30 May 2019; Accepted: 24 June 2019; Published: 26 June 2019



**Abstract:** The structure sensitivity of the alkaline oxygen reduction reaction (ORR) on palladium is of great interest as cost considerations drive the need to find a replacement for platinum catalysts. The kinetics of alkaline ORR were investigated on nanocrystalline palladium (Pd) films with domain sizes between 14 and 30 nm that were synthesized by electrodeposition from aqueous electrolytes. Ten Pd films were prepared under varying electrodeposition parameters leading to each having a unique texture and morphology. The sensitivity of initial alkaline ORR kinetics to the Pd surface structure was evaluated by measuring the kinetic current density and number of electrons transferred for each film. We show through scanning electron microscopy (SEM), x-ray diffraction (XRD), atomic force microscopy (AFM), and voltammetry from rotating disc electrodes (RDEs) that the fastest alkaline ORR kinetics are found on Pd surfaces with high surface roughness, which themselves are composed of fine grains. Such a study is useful for developing membrane electrode assemblies (MEAs) based on directly electrodepositing catalyst onto a conductive diffusion layer.

**Keywords:** Pd thin films; electrocatalysis; electrodeposition

## 1. Introduction

Broad fuel cell commercialization efforts can be frustrated by prohibitively high costs and insufficient durability, which is attributed mainly to challenges in catalyst development [1]. Compared to the acidic polymer electrolyte membrane fuel cell (PEMFC), alkaline fuel cells show relatively fast kinetics for the oxygen reduction reaction (ORR). Consequently, the development of platinum-free cathodes for alkaline fuel cells has been of great interest owing to the high cost and limited availability of platinum (Pt) [2–5]. Palladium (Pd), as a pure metal, is a good candidate to substitute for Pt cathodes in alkaline membrane fuel cells (AMFCs), as its performance as a catalyst for ORR in alkaline media exceeds its performance in acidic media [6]. A recent study on the relationship between alkaline ORR catalytic activity and the metal d-band center showed that Pd(111)-terminated nanoparticles and nano-Pd/C both had a d-band center value close to Pt(111)-terminated nanoparticles and Pt/C respectively, suggesting that Pd may offer a viable replacement for Pt in fuel cells [7,8]. Pd mining resources are also comparable to those for platinum; typically 2–3 fold less expensive than Pt.

It is well understood that the structure of the catalytic surface can play just as significant a role in the observed kinetic rate as the atomic composition [9–11]. The focus of developing Pt-free cathodes has therefore been redirected in the last 10 years towards elucidating the structural sensitivity of catalysts used in commercial fuel cells. These studies generally fall into one of two categories: polished single crystal surfaces or faceted nanoparticles whose faces are terminated by a single crystallographic plane (e.g., (100)-terminated FCC nanoparticles will make cube [12,13]). While polished single crystal surfaces are easily characterized and reproducible, they do not represent a realistic catalyst system. Alternatively, faceted nanoparticles more closely resemble commercial catalysts; however, it is difficult

to identify structural variations between individual particles over such a large scale. As opposed to structural studies of Pt and Pd in acidic electrolytes [9,14,15], the role of Pd structure on alkaline ORR kinetics remains unclear.

Erikson et al. report that 5 nm (100)-terminated Pd nanocubes outperformed their polycrystalline spherical counterparts, leading them to conclude that a structural sensitivity existed and Pd(100) was the most active plane [12]. By contrast, Shao et al. reported no structural dependence between Pd(100)-terminated cubes and Pd(111)-terminated octahedra, although it should be noted that the nanoparticles in the this study were reported to be 27 nm, 5 times larger than the Erikson study [16]. Such a conflict is representative of the lack of clarity for evaluating the structural dependence of Pd on alkaline ORR kinetics. Work from Jiang et al. suggested that the structural difference may be due to a size dependence rather than preferred orientation. They report a 3-fold increase in alkaline ORR kinetics as the nanoparticle size increased from 3 to 16 nm [17].

By comparison to single-crystal and nanoparticle studies of alkaline ORR activity, the use of electrodeposition of nanocrystalline films is less studied, but an emerging method for building fuel cell membrane electrode assemblies (MEA). Using this method, the catalyst is directly electrodeposited onto the gas diffusion layer (GDL) and is then hot-pressed in contact with the ionically conductive membrane [18]. Here, we employ pulse and direct current electrodeposition from aqueous electrolytes to synthesize nanocrystalline Pd films with varying roughness and morphology. Structural sensitivity is evaluated by comparing the average structural properties of each film to its alkaline ORR performance.

## 2. Results and Discussion

### 2.1. Sample Preparation

Pd films having various morphologies and textures were prepared by electrodeposition onto gold disc electrodes using either direct current (DC) or pulse current (PC) electrodeposition. In the case of PC deposition, the peak current density and duty cycle were varied. The duty cycle is defined as the percentage of the total pulse width where the current is on. A summary of the samples prepared for this study is shown in Table 1. All surfaces were prepared at room temperature and limited to a total charge of 1.5 C/cm<sup>2</sup>.

**Table 1.** Deposition parameters for controlling Pd film morphology.

Peak Current Density [mA/cm <sup>2</sup> ]	Direct Current (DC) or Pulse Current (PC) Deposition	Pulse Width (ms)	ECSA (cm <sup>2</sup> )† Pd-O Reduction
30	PC; 20% duty cycle	100	0.280
30	PC; 35% duty cycle	100	0.261
30	PC; 50% duty cycle	100	0.199
3	DC	-	0.384
3	PC; 20% duty cycle	100	0.690
3	PC; 35% duty cycle	100	0.417
3	PC; 50% duty cycle	100	0.480
10	DC	-	0.423
20	DC	-	0.494
30	DC	-	0.608

† The geometric surface area of the gold disc was 0.196 cm<sup>2</sup>.

## 2.2. Electrochemical Surface Area Characterization

After electrodeposition, the electrochemical surface area (ECSA) of the Pd film was calculated by measuring the charge required to reduce a monolayer of palladium oxide in a method similar to the one reported for Pd-Cu alloy films [19]. Briefly, a cyclic voltammogram was taken in an N<sub>2</sub>-saturated 0.1 M HClO<sub>4</sub> electrolyte between 0.4 V vs. the reversible hydrogen electrode (RHE) and a variable positive inversion potential. This inversion potential was varied and plotted against the charge associated with palladium oxide reduction. At the inversion potential associated with the formation of a single monolayer of palladium oxide (1.544 V vs. RHE), a slope change is observed (Figure S1) representing the transition between monolayer and multilayer formation. The ECSA was calculated by Equation (1) at this inversion potential where Q<sub>M</sub> is the charge required to reduce a monolayer of palladium oxide.

$$ECSA[\text{cm}^2] = \frac{Q_M[\text{C}] \times 10^6}{405\left[\frac{\text{C}}{\text{cm}^2}\right]} \quad (1)$$

Previous reports have shown that the repeated formation and reduction of palladium oxides can impact the surface roughness through the formation of multi-dimensional defects such as grain boundaries and clusters of adatoms, zero-dimensional defects such as vacancies, as well as drive atomic rearrangement [20]. Since this the ECSA measurement procedure involved the 1-time formation of an oxide monolayer and its subsequent reduction, the modulation of the surface roughness via the formation of the monolayer oxide is believed to be minimal. Alternative methods for measuring the ECSA include evaluation of the hydrogen stripping region, and the removal of a copper (Cu) monolayer placed on top of palladium by underpotential deposition (UPD).

It is well known that the hydrogen region on palladium electrodes exhibits poor definition, mostly due to the fact that hydrogen is both adsorbed and absorbed owing to its high solubility. Figure S2 shows the cyclic voltammograms, including the hydrogen adsorption/desorption regions, for the samples prepared in this work. Since it was difficult to unambiguously define the hydrogen region on our Pd films, the ECSA values using this procedure are not reported. Cu UPD has also been previously used to define the ECSA of both polycrystalline and single crystal electrodes [21–23]. Consistent with these reports, this technique was found to give ECSA values 150%–200% larger than that of the other methods. Furthermore, in polycrystalline Pd films, structural determination from Cu UPD is difficult to extract because the contribution of the different planes to the atomic arrangement of the surface is not known. In consideration of the above and the fact that the reduction of Pd-O gave the most reproducible results, we report ECSA values using this technique in Table 1.

## 2.3. Structural Characterization of Pd Films

Scanning electron microscopy (SEM) images were taken to show how changing palladium electrodeposition parameters gave rise to different morphologies. Figure 1 shows a series of Pd films that were deposited at 3 mA/cm<sup>2</sup> at various duty cycles. All surfaces appeared to be compact and have a needle-like morphology.

By comparing Figure 1a–d, it is shown that the needle-like characteristic became enhanced as the duty cycle increased from 20% to 100% (DC). Figure 2 shows SEM micrographs of Pd films electrodeposited at 30 mA/cm<sup>2</sup> at various duty cycles. It is clear that the morphology of these samples differed from those deposited at 3 mA/cm<sup>2</sup>. As the duty cycle increased, the morphology of the film transitioned from a coalesce (globular) structure to a faceted structure.

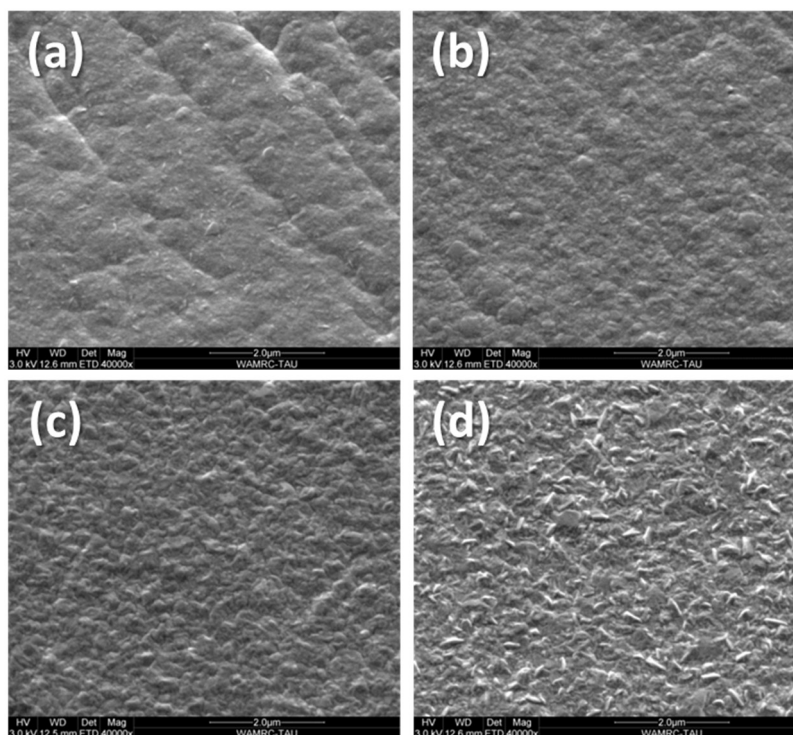


**Figure 1.** Scanning electron microscopy (SEM) images of Pd films deposited at 3 mA/cm<sup>2</sup> (a) 20% duty cycle (b) 35% duty cycle (c) 50% duty cycle (d) DC (100% duty cycle).

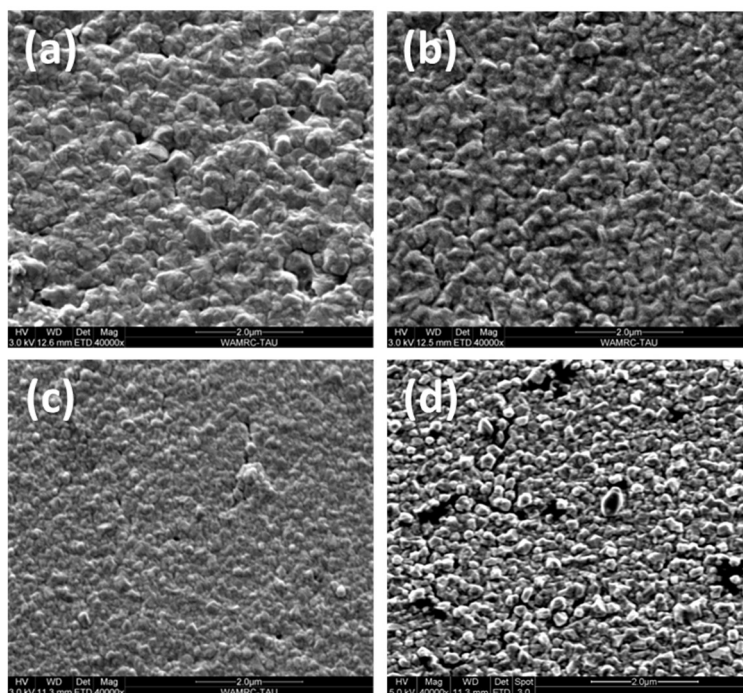


**Figure 2.** Scanning electron microscope (SEM) images of Pd films deposited at 30 mA/cm<sup>2</sup> (a) 20% duty cycle (b) 35% duty cycle (c) 50% duty cycle (d) DC (100% duty cycle).

Pd-films prepared by DC electrodeposition at 10 mA/cm<sup>2</sup>, 20 mA/cm<sup>2</sup> appeared to have a faceted morphology similar to the 30 mA/cm<sup>2</sup> DC sample (Figure S3). In all cases, films deposited at above 10 mA/cm<sup>2</sup> were less compact compared to films deposited at 3 mA/cm<sup>2</sup>. Morphology changes observed in Figures 1 and 2 are related to the sensitivity of the nucleation and crystallization processes to the depletion of Pd ions in the boundary layer adjacent to the gold disc. Both the current density and the duty

cycle therefore served to modulate the mass-transfer and kinetics of Pd film electrodeposition [24,25]. When growth is the dominant mechanism, the surface consists of large and coarse deposits whereas when the nucleation processes dominate, the surface is smooth. Assuming the limiting current density is not exceeded, DC deposition is expected to yield smaller crystallites compared to PC deposition at the same average current density because grain growth takes place during the relaxation time. For instance, the Pd film deposited at 10 mA/cm<sup>2</sup> under DC conditions and the one deposited at 30 mA/cm<sup>2</sup> with a duty cycle of 35% both had an average current density of ~10 mA/cm<sup>2</sup>, yet the PC sample gave grains ~35% larger.

When the pulse limiting current density for Pd deposition in this electrolyte (18.2 mA/cm<sup>2</sup>, Figure S4) was exceeded, as was the case for Pd films prepared at 20 and 30 mA/cm<sup>2</sup>, side reactions including hydrogen evolution, local changes in pH, and a thicker diffusion layer all served to interrupt and impede growth, giving rise to smaller crystallites. The replenishment of Pd ions during the relaxation time increased the instantaneous limiting current density achievable using PC deposition compared to the limiting current density observed in DC deposition [26]. Therefore, decreasing the duty cycle (increasing the relaxation time) served to increase the pulse limiting current density and reduced the occurrence of processes serving to interrupt growth. This in turn led to larger crystallites with decreasing duty cycle.

#### 2.4. Alkaline ORR Characterization

The electrochemical reduction of O<sub>2</sub> on nanocrystalline Pd films was studied in oxygen-saturated 0.1 M KOH solutions using rotating disk electrodes. Figure 3a shows a characteristic cathodic linear sweep voltammograms (LSV) starting from 1 V to 0.3 V vs. RHE at 10 mV/s at different rotation rates. Although only the Pd film deposited at DC 10 mA/cm<sup>2</sup> is shown here, this figure is representative of all Pd films in this study. The remaining plots are shown in (Figures S5–S7).

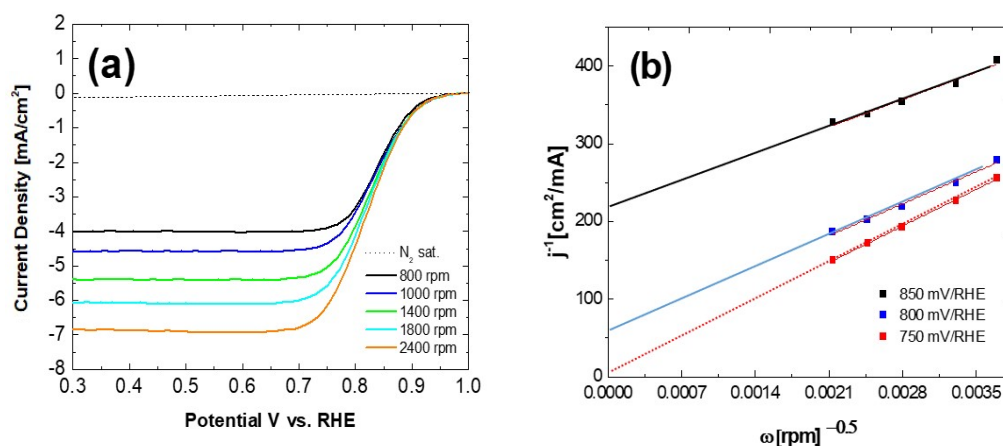


**Figure 3.** (a) ORR polarization curves for the Pd film prepared at 10 mA/cm<sup>2</sup> DC at different rotation speeds, scan rate 10 mA/s (b) Koutecky–Levich plot for Pd film deposited at 10 mA/cm<sup>2</sup> DC.

The RDE data was fit to the Koutecky–Levich (K–L) equation (Equation (2))

$$\frac{1}{j} = \frac{1}{j_k} + \frac{1}{j_l} = \frac{1}{j_k} + \frac{1}{0.62nFAD_0^{2/3}\nu^{-1/6}C^*\omega^{1/2}} \quad (2)$$

where  $j$  is the current density,  $j_k$  is the kinetic current density,  $j_l$  is the limiting current density,  $F$  is 96,484.56 C mol<sup>-1</sup>,  $n$  is the number of electrons transferred,  $A$  is the area in cm<sup>2</sup>,  $D$  is the diffusion coefficient of O<sub>2</sub> in cm<sup>2</sup> s<sup>-1</sup>,  $C^*$  is the bulk concentration of O<sub>2</sub> in mol cm<sup>-3</sup>,  $\nu$  is kinematic viscosity in cm<sup>2</sup> s<sup>-1</sup>, and  $\omega$  is the rotation rate in rpm. The coefficients used for 0.1 M KOH electrolyte at 30 °C were:  $D = 1.9 \times 10^{-5}$  cm<sup>2</sup> s<sup>-1</sup>,  $C^* = 1.1 \times 10^{-6}$  mol cm<sup>-3</sup>, and  $\nu = 1.3 \times 10^{-2}$  cm<sup>2</sup> s<sup>-1</sup> [27]. Figure 3b shows

that the fit to Equation (2) at 750, 800, and 850 mV vs. RHE is linear, indicating first-order kinetics with respect to molecular oxygen. Koutecký–Levich fitting for the remaining samples are shown in Figures S8–S10. The initial kinetic current density for alkaline ORR,  $j_k$ , a characteristic indicator of the reaction's kinetics, is derived from the slope of the fitted lines [6].

### 2.5. Effect of Pd Morphology and Texture on Alkaline ORR Kinetics

In order to characterize the relationship between alkaline ORR kinetics and structure sensitivity, key structural parameters including morphology, weighted grain size, and roughness factor (electrochemical surface area divided by geometrical area) were correlated with the initial kinetics of alkaline oxygen reduction as characterized by the sample's kinetic current density and number of electrons transferred.

To better visualize these relationships, 2D meshes were created, where the axes are two selected descriptions of the surface, and the color map displays the kinetic variable. Figure 4 shows how the number of electrons transferred and the kinetic current density varied with weighted grain size and roughness factor at 750 mV vs. RHE. The weighed grain size is the sum total of the grain size of each Pd crystal orientation multiplied by the relative abundance of that orientation.

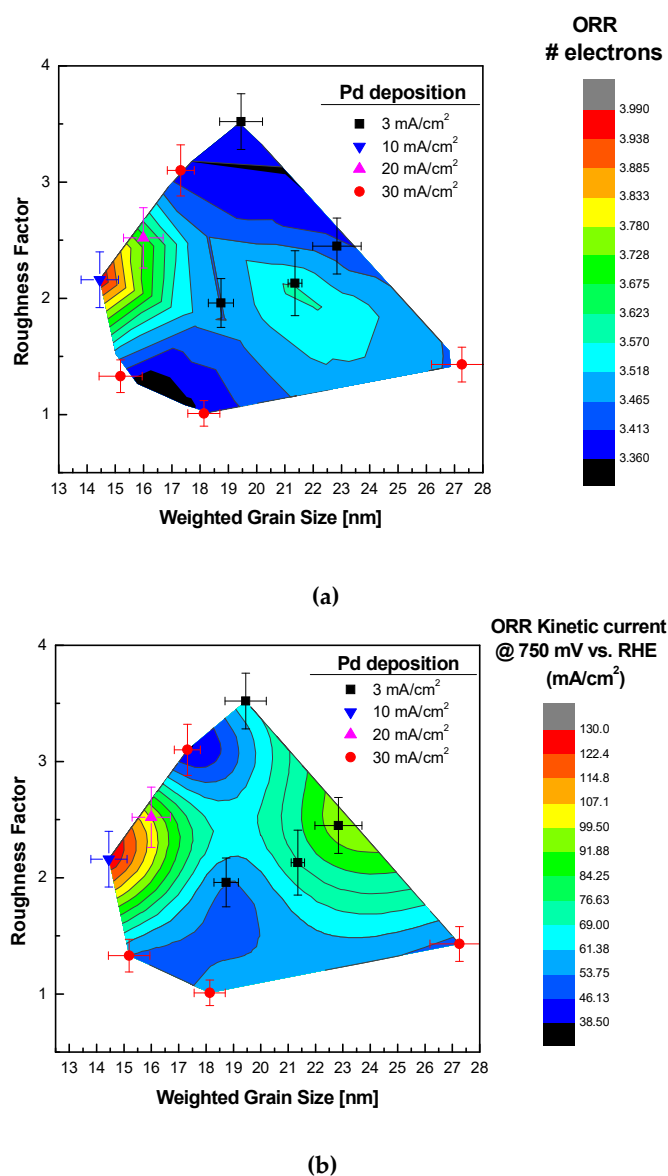


**Figure 4.** (a) Number of electrons transferred and (b) kinetic current density and number of electrons at 750 mV vs. RHE as function of the weighted grain size and roughness factor.

As the weighted grain size decreased, both the kinetic current density and number of electrons transferred increased. This trend can be explained by the fact that smaller grains necessarily lead to a larger density of grain boundaries. Grain boundaries can often break the translation symmetry in the direction perpendicular to the contact interface. This gives rise to strongly localized electronic states in the vicinity of the grain boundary and to the redistribution of the electronic charge density, making the electron density less uniform. The non-uniformity of charge distribution in the neighborhood of grain boundaries may be considered as a type of dangling bond stimulating the charge transfer from the substrate to the adsorbate, thereby enhancing adsorption and reaction kinetics [28].

At a fixed grain size, a local maximum is observed in the kinetic current density as the roughness factor is varied. Such a "volcano" behavior may be indicative of how surface roughness influences the Pd-O bond strength and therefore reduction kinetics via Sabatier's principle [29]. From Figure 4, we conclude that both the roughness factor and the weighted grain size influence the kinetic current density and the oxygen reduction mechanism (via the number of electrons transferred).

The mixed contribution of film morphology and microtexture is visualized in Figure 5. The morphology of the Pd film is defined by SEM images shown earlier as being either compact needle-like, coalesce, or faceted. Although the kinetic current density does not globally increase in a linear fashion with decreasing grain size, the impact of grain size on the kinetic current density appears more linear when comparing between samples of the same morphology.

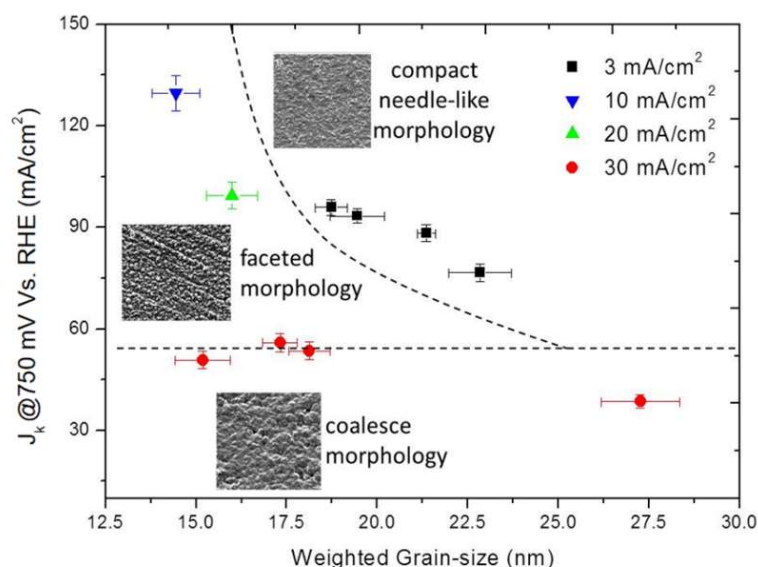


**Figure 5.** Structural phase diagram showing the kinetic current density at 750 mV vs. RHE as function of weighted grain size and morphology.

Atomic force microscopy (AFM) shown in Figure 6 was used to distinguish between the different morphological groups by their average surface roughness ( $S_a$ ) evaluated over the complete 3D surface [30]. Mathematically,  $S_a$  is defined as:

$$S_a = \frac{1}{A} \iint_a |Z(x, y)| dx dy \quad (3)$$

where larger values of  $S_a$  indicate rougher surfaces.

The faceted morphology had the largest  $S_a$  value (0.588  $\mu\text{m}$ ), meaning it has the roughest surface. As expected, the compact needle-like morphology had the lowest  $S_a$  (0.179  $\mu\text{m}$ ), and coalesce gave an intermediate  $S_a$  value between the faceted and compact values (0.271  $\mu\text{m}$ ).

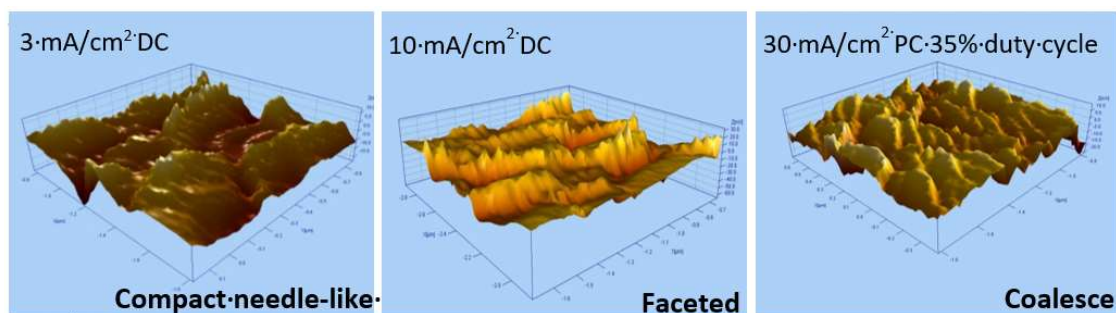


**Figure 6.** Atomic force microscopy (AFM) maps of needle-like, faceted, and coalesce domains in the Pd film.

### 3. Experimental

#### 3.1. Electrochemistry

Cyclic voltammetry (CV) was carried out using a rotating disk electrode (RDE) in 0.1 M KOH (Merck Co) placed inside a jacketed three-electrode cell. All electrolytes were kept at 303 K by a heated bath recirculator. The electrolyte was purged with N<sub>2</sub> or O<sub>2</sub> by flowing 120 sccm of the appropriate gas through a glass frit placed in the electrolyte for 30 min. Electrochemical control was through a BioLogic VSP-300 potentiostat. After electropolishing, linear sweep voltammograms (LSV) were taken from 1 V to 0.3 V vs. RHE at a scan rate of 10 mV/s at varying rotation speeds (0, 800, 1000, 1400, 1800, and 2400 rpm). Reported LSV curves are the fifth in a series of five consecutively acquired LSVs in order to ensure a stable profile.

#### 3.2. Materials Characterization

Scanning electron microscopy (SEM) (ThermoFisher, Waltham, MA, USA,) micrographs were taken by a Quanta 200 FEG (field-emission gun) Environmental Scanning Electron Microscope (ESEM) operated in high-vacuum mode. The sample stage was tilted to 20° during sample examination in order to minimize capacitance effects. The electron beam voltage was at 3.5 keV. Atomic force microscopy (AFM, PicoSPMTM, Molecular Imaging) was used to image the surfaces in air. Imaging was done by using tips made of Si<sub>3</sub>N<sub>4</sub> (Veeco) in contact-mode. Following the image processing, surface roughness parameters were calculated with the aid of SPIPTM software.

Analysis of the grain size in the Pd films were characterized using the D8 Advance diffractometer (Bruker, Karlsruhe, Germany) using Cu Ka1 radiation ( $k = 1.540562$ ). XRD patterns were collected from  $2\theta$  of 20° to 110° at a scan speed of 1.0/min and at a grazing incident angle of 2° to minimize the contribution from the gold substrate. Although the grain size measured by XRD is measured perpendicular to the surface, grain size measurements from electron backscatter diffraction (EBSD) parallel to the surface were found to be in good agreement with XRD.

### 4. Conclusions

Electrodeposited nanocrystalline Pd films were shown to be active for ORR in alkaline media. The influence of electrodeposition parameters was found to influence the surface morphology and weighed grain size, resulting in Pd surfaces displaying different ORR kinetics. The influence of grain size and surface roughness were found to have a profound impact on the reduction of oxygen. This is likely due to the impact of grain boundaries on oxygen adsorption. In practice, we find that ORR kinetics can be maximized by depositing a surface that has both a large surface roughness and composed of a fine-grained structure with many grain boundaries. Within the range of parameters observed, the Pd film that performed the best was deposited at DC 10mA/cm<sup>2</sup>. By contrast, the film that performed the worst was the one prepared at 30mA/cm<sup>2</sup> PC and 20% duty cycle owing to its large grains and smooth morphology.

**Supplementary Materials:** The following are available online at <http://www.mdpi.com/2073-4344/9/7/566/s1>, **Figure S1.** (a) Cyclic voltammograms at several inversion potential ( $E_{inv}$  in the inset) for the 20 mA/cm<sup>2</sup> DC sample with N<sub>2</sub> saturated H<sub>2</sub>SO<sub>4</sub> (0.5M) solution. Scan rate of 50 mV/s. The arrow indicating the Pd reduction peak. (b) Plot of the oxide reduction charge against the inversion potential ( $E_{inv}$ ) for the 20 mA/cm<sup>2</sup> DC sample. The intercept between the lines stands for the charge for an oxide monolayer reduction. **Figure S2:** Cyclic voltammetry showing the hydrogen region for each of the Pd films in 0.5M H<sub>2</sub>SO<sub>4</sub> at a sweep rate of 10 mV/s. **Figure S3.** ESEM images of Pd films deposited at (a) 10 mA/cm<sup>2</sup> x40k (B) 20 mA/cm<sup>2</sup> x40k. **Figure S4.** Linear sweep voltammetry of gold electrode in the Pd deposition solution, limiting current density is reached at 18.2 mA/cm<sup>2</sup>. **Figure S5.** polarization curves of ORR at different rotation speed, scan rate:10 mA/s: (A)3 mA/cm<sup>2</sup> 20% duty cycle (B) 3 mA/cm<sup>2</sup> 35% duty cycle (C) 3 mA/cm<sup>2</sup> 50% duty cycle (D) 3 mA/cm<sup>2</sup> DC. **Figure S6.** polarization curves of ORR at different rotation speed, scan rate:10 mA/s: (A) 30 mA/cm<sup>2</sup> 20% duty cycle (B) 30 mA/cm<sup>2</sup> 35% duty cycle (C) 30 mA/cm<sup>2</sup> 50% duty cycle (D) 30 mA/cm<sup>2</sup> DC. **Figure S7.** polarization curves of ORR at different rotation speed, scan rate:10 mA/s: (A) 10 mA/cm<sup>2</sup> DC (B) 20 mA/cm<sup>2</sup> DC. **Figure S8.** K–L plots of each sample replotted at different voltages: (A) 3 mA/cm<sup>2</sup> 20% duty cycle (B) 3 mA/cm<sup>2</sup> 35% duty cycle (C) 3 mA/cm<sup>2</sup> 50% duty cycle (D) 3 mA/cm<sup>2</sup> DC. **Figure S9.** K–L plots of each sample replotted at different voltages: (A)30 mA/cm<sup>2</sup> 20% duty cycle (B) 30 mA/cm<sup>2</sup> 35% duty cycle (C) 30 mA/cm<sup>2</sup> 50% duty cycle (D) 30 mA/cm<sup>2</sup> DC. **Figure S10.** K–L plots of each sample replotted at different voltages: (A) 10 mA/cm<sup>2</sup> DC (B) 20 mA/cm<sup>2</sup> DC.

**Author Contributions:** B.A.R. and E.H. conceived and designed the experiments; E.H. and A.R. performed the experiments; E.H. and A.R. analyzed the data; B.A.R. drafted the paper with critical comments from the other authors.

**Funding:** This research received no external funding.

**Acknowledgments:** The authors would like to acknowledge the support of the Planning & Budgeting Committee/ISRAEL Council for Higher Education (CHE) and Fuel Choice Initiative (Prime Minister Office of ISRAEL), within the framework of “Israel National Research Center for Electrochemical Propulsion” (INREP).

**Conflicts of Interest:** The authors declare no conflict of interest.

## References

1. Gasteiger, H.A.; Kocha, S.S.; Sompalli, B.; Wagner, F.T. Activity benchmarks and requirements for Pt, Pt-alloy, and non-Pt oxygen reduction catalysts for PEMFCs. *Appl. Catal. B Environ.* **2005**, *56*, 9–35. [[CrossRef](#)]
2. Shao, M. Palladium-based electrocatalysts for hydrogen oxidation and oxygen reduction reactions. *J. Power Sour.* **2011**, *196*, 2433–2444. [[CrossRef](#)]
3. Henning, S.; Herranz, J.; Gasteiger, H.A. Bulk-Palladium and Palladium-on-Gold Electrocatalysts for the Oxidation of Hydrogen in Alkaline Electrolyte. *J. Electrochem. Soc.* **2015**, *162*, F178–F189. [[CrossRef](#)]
4. Durst, J.; Siebel, A.; Simon, C.; Hasché, F.; Herranz, J.; Gasteiger, H.A. New insights into the electrochemical hydrogen oxidation and evolution reaction mechanism. *Energy Environ. Sci.* **2014**, *7*, 2255–2260. [[CrossRef](#)]
5. Sheng, W.; Bivens, A.P.; Myint, M.; Zhuang, Z.; Forest, R.V.; Fang, Q.; Chen, J.; Yan, Y. Non-precious metal electrocatalysts with high activity for hydrogen oxidation reaction in alkaline electrolytes. *Energy Environ. Sci.* **2014**, *7*, 1719–1724. [[CrossRef](#)]
6. Srejić, I.; Rakocević, Z.; Nenadović, M.; Strbac, S. Oxygen reduction on polycrystalline palladium in acid and alkaline solutions: Topographical and chemical Pd surface changes. *Electrochim. Acta* **2015**, *169*, 22–31. [[CrossRef](#)]
7. Lima, F.H.B.; Zhang, J.; Shao, M.H.; Sasaki, K.; Vukmirovic, M.B.; Ticianelli, E.A.; Adzic, R.R. Catalytic Activity–d-Band Center Correlation for the O<sub>2</sub> Reduction Reaction on Platinum in Alkaline Solutions. *J. Phys. Chem. C* **2007**, *111*, 404–410. [[CrossRef](#)]
8. Shao, M.-H.; Sasaki, K.; Adzic, R.R. Pd–Fe Nanoparticles as Electrocatalysts for Oxygen Reduction. *J. Am. Chem. Soc.* **2006**, *128*, 3526–3527. [[CrossRef](#)]
9. Marković, N.; Adzic, R.R.; Cahan, B.D.; Yeager, E.B. Structural effects in electrocatalysis: Oxygen reduction on platinum low index single-crystal surfaces in perchloric acid solutions. *J. Electroanal. Chem.* **1994**, *377*, 249–259. [[CrossRef](#)]
10. Poirier, J.A.; Stoner, G.E. Microstructural Effects on Electrocatalytic Oxygen Reduction Activity of Nano-Grained Thin-film Platinum in Acid Media. *J. Electrochem. Soc.* **1994**, *141*, 425–430. [[CrossRef](#)]
11. Yoon, Y.-G.; Park, G.G.; Yang, T.H.; Han, J.N.; Lee, W.Y.; Kim, C.S. Effect of pore structure of catalyst layer in a PEMFC on its performance. *Int. J. Hydrog. Energy* **2003**, *28*, 657–662. [[CrossRef](#)]

12. Erikson, H.; Merisalu, M.; Rähn, M.; Sammelseg, V.; Tammeveski, K. Electrochemical reduction of oxygen on palladium nanocubes in acid and alkaline solutions. *Electrochim. Acta* **2012**, *59*, 329–335. [[CrossRef](#)]
13. Marks, L.; Peng, L. Nanoparticle shape, thermodynamics and kinetics. *J. Phys. Condens. Matter* **2016**, *28*, 53001. [[CrossRef](#)] [[PubMed](#)]
14. Markovic, N.M.; Gasteiger, H.A.; Ross, P.N. Oxygen reduction on platinum low-index single-crystal surfaces in alkaline solution: Rotating ring diskPt (hkl) studies. *J. Phys. Chem.* **1996**, *100*, 6715–6721. [[CrossRef](#)]
15. Kondo, S.; Nakamura, M.; Maki, N.; Hoshi, N. Active sites for the oxygen reduction reaction on the low and high index planes of palladium. *J. Phys. Chem. C* **2009**, *113*, 12625–12628. [[CrossRef](#)]
16. Shao, M.; Odell, J.; Humbert, M.; Yu, T.; Xia, Y. Electrocatalysis on shape-controlled palladium nanocrystals: Oxygen reduction reaction and formic acid oxidation. *J. Phys. Chem. C* **2013**, *117*, 4172–4180. [[CrossRef](#)]
17. Jiang, L.; Hsu, A.; Chu, D.; Chen, R. Size-dependent activity of palladium nanoparticles for oxygen electroreduction in alkaline solutions. *J. Electrochem. Soc.* **2009**, *156*, B643–B649. [[CrossRef](#)]
18. Litster, S.; McLean, G. PEM fuel cell electrodes. *J. Power Sour.* **2004**, *130*, 61–76. [[CrossRef](#)]
19. Fouda-Onana, F.; Bah, S.; Savadogo, O. Palladium–copper alloys as catalysts for the oxygen reduction reaction in an acidic media I: Correlation between the ORR kinetic parameters and intrinsic physical properties of the alloys. *J. Electroanal. Chem.* **2009**, *636*, 1–9. [[CrossRef](#)]
20. Grdeń, M.; Łukaszewski, M.; Jerkiewicz, G.; Czerwiński, A. Electrochemical behaviour of palladium electrode: Oxidation, electrodisolution, and ionic adsorption. *Electrochim. Acta* **2009**, *53*, 7583–7598.
21. Mayet, N.; Servat, K.; Kokoh, B.; Napporn, T.W. Probing the Surface of Noble Metals Electrochemically by Underpotential Deposition of Transition Metals. *Surfaces* **2019**, *2*, 257–276. [[CrossRef](#)]
22. Chierchie, T.; Mayer, C. Voltammetric study of the underpotential deposition of copper on polycrystalline and single crystal palladium surfaces. *Electrochim. Acta* **1988**, *33*, 341–345. [[CrossRef](#)]
23. Shao, M.; Odell, J.H.; Choi, S.; Xia, Y. Electrochemical surface area measurements of platinum- and palladium-based nanoparticles. *Electrochem. Commun.* **2013**, *31*, 46–48. [[CrossRef](#)]
24. Natter, H.; Hempelmann, R.; Krajewski, T. Nanocrystalline Palladium by Pulsed Electrodeposition. *Berichte der Bunsengesellschaft für physikalische Chemie* **1996**, *100*, 55–64. [[CrossRef](#)]
25. Fukumoto, Y.; Kawashima, Y.; Hayashi, T. Pulse plating of Pd-Ni alloys: Dependence on current density. *Surf. Coat. Tech.* **1986**, *27*, 145–150. [[CrossRef](#)]
26. Rosen, B.A.; Gileadi, E.; Eliaz, N. Microstructure and composition of pulse plated Re–Ni alloys on a rotating cylinder electrode. *J. Electroanal. Chem.* **2014**, *731*, 93–99. [[CrossRef](#)]
27. Xing, W.; Yin, M.; Lv, Q.; Hu, Y.; Liu, C.; Zhang, J. 1-Oxygen Solubility, Diffusion Coefficient, and Solution Viscosity. In *Rotating Electrode Methods and Oxygen Reduction Electrocatalysts*; Elsevier: Amsterdam, The Netherlands, 2014; pp. 1–31.
28. Crampin, S.; Vvedensky, D.D.; MacLaren, J.M.; Eberhart, M.E. Electronic structure near (210) tilt boundaries in nickel. *Phys. Rev. B.* **1989**, *40*, 3413. [[CrossRef](#)]
29. Lavacchi, A.; Miller, H.; Vizza, F. *Nanotechnology in Electrocatalysis for Energy*; Springer: New York, NY, USA, 2013.
30. De Oliveira, R.R.L.; Albuquerque, D.A.C.; Cruz, T.G.S.; Yamaji, F.M.; Leite, F.L. Measurement of the Nanoscale Roughness by Atomic Force Microscopy: Basic Principles and Applications, Atomic Force Microscopy—Imaging, Measuring and Manipulating Surfaces at the Atomic Scale, Victor Bellitto, IntechOpen, doi:10.5772/37583. Available online: <https://www.intechopen.com/books/atomic-force-microscopy-imaging-measuring-and-manipulating-surfaces-at-the-atomic-scale/measurement-of-the-nanoscale-roughness-by-atomic-force-microscopy-basic-principles-and-applications> (accessed on 26 June 2019).

